N-[*N*-[(*S*)-1,3-Dicarboxypropyl]Carbamoyl]-4-[^{18}F]Fluorobenzyl-L-Cysteine, [^{18}F]DCFBC: A New Imaging Probe for Prostate Cancer

Ronnie C. Mease,[1] Crystal L. Dusich,[1] Catherine A. Foss,[1] Hayden T. Ravert,[1] Robert F. Dannals,[1] Jurgen Seidel,[1] Andrew Prideaux,[1] James J. Fox,[1] George Sgouros,[1] Alan P. Kozikowski,[2] and Martin G. Pomper[1]

Abstract

Purpose: Previously, we showed successful imaging of xenografts that express the prostate-specific membrane antigen (PSMA) using small-animal positron emission tomography (PET) and the radiolabeled PSMA inhibitor *N*-[*N*-[(*S*)-1,3-dicarboxypropyl]carbamoyl]-*S*-[^{11}C]methyl-L-cysteine. Herein, we extend that work by preparing and testing a PSMA inhibitor of the same class labeled with fluorine-18.

Experimental Design: *N*-[*N*-[(*S*)-1,3-Dicarboxypropyl]carbamoyl]-4-[^{18}F]fluorobenzyl-L-cysteine ([^{18}F]DCFBC) was prepared by reacting 4-[^{18}F]fluorobenzyl bromide with the precursor (*S*)-2-[3-[(*R*)-1-carboxy-2-mercaptoethyl]ureido]-pentanedioic acid in ammonia-saturated methanol at 60°C for 10 min followed by purification using C-18 reverse-phase semipreparative high-performance liquid chromatography. Severe combined immunodeficient mice bearing a s.c. PSMA$^+$ PC-3 PIP tumor behind one shoulder and a PSMA$^-$ PC-3 FLU tumor behind the other shoulder were injected via the tail vein with either 1.85 MBq (50 μCi) of [^{18}F]DCFBC for *ex vivo* biodistribution or 7.4 MBq (200 μCi) for imaging. For biodistribution, mice were sacrificed at 5, 15, 30, 60, and 120 min. Tumor, blood, and major organs were harvested and weighed, and radioactivity was counted. Imaging was done on the GE eXplore Vista small-animal PET scanner by collecting 12 consecutive 10-min frames.

Results: Radiochemical yield for [^{18}F]DCFBC averaged 16 ± 6% (n = 8) from 4-[^{18}F]fluorobenzyl bromide. Specific radioactivities ranged from 13 to 133 GBq/μmol (350-3,600 Ci/mmol) with an average of 52 GBq/μmol (1,392 Ci/mmol; n = 6). Biodistribution and imaging studies showed high uptake of [^{18}F]DCFBC in the PIP tumors with little to no uptake in FLU tumors. High radiopharmaceutical uptake was also seen in kidneys and bladder; however, washout of radioactivity from these organs was faster than from the PIP tumors. The maximum PIP tumor uptake was 8.16 ± 2.55% injected dose per gram, achieved at 60 min after injection, which decreased to 4.69 ± 0.89 at 120 min. The PIP tumor to muscle ratio was 20 at 120 min after injection. Based on the mouse biodistribution, the dose-limiting organ is the kidneys (human estimated absorbed dose: 0.05 mGy/MBq; 0.2 rad/mCi).

Conclusion: [^{18}F]DCFBC localizes to PSMA$^+$-expressing tumors in mice, permitting imaging by small-animal PET. This new radiopharmaceutical is an attractive candidate for further studies of PET imaging of prostate cancer.

Prostate cancer is the leading cancer in the U.S. population and second leading cause of cancer death in men (1). Staging of the disease becomes more important as new therapeutic options, such as thermal ablation or high-intensity focused ultrasound, become available. Staging can be done noninvasively with imaging, and several experimental radiopharmaceuticals are under evaluation (2–5). One important indication for imaging prostate cancer is to determine the location of recurrence in patients who have undergone prostatectomy who present with rising prostate-specific antigen (PSA). That is the indication for using ProstaScint, a monoclonal antibody–based imaging agent that binds to the prostate-specific membrane antigen (PSMA; ref. 6). We have also been interested in PSMA as an imaging target not only to detect prostate cancer (7–9) but also because PSMA is up-regulated in the neovasculature of many tumor types (10). That latter characteristic of PSMA has recently been exploited in monoclonal antibody–based imaging of solid tumors other than prostate (11).

In our effort to develop a PSMA-based imaging agent of low molecular weight for positron emission tomography (PET) with more widespread utility (i.e., a longer physical half-life and potentially better pharmacokinetic characteristics), we have extended our previous work with the carbon-11–labeled

Authors' Affiliations: [1]Russell H. Morgan Department of Radiology, Johns Hopkins Medical Institutions, Baltimore, Maryland and [2]Department of Medicinal Chemistry and Pharmacognosy, University of Illinois at Chicago, Chicago, Illinois
Received 6/19/07; revised 8/13/07; accepted 9/28/07.

Grant support: U24 CA92871 R21 EB005324, R21 CA111982, PC050825, AdMeTech and P50 103175.

The costs of publication of this article were defrayed in part by the payment of page charges. This article must therefore be hereby marked *advertisement* in accordance with 18 U.S.C. Section 1734 solely to indicate this fact.

Requests for reprints: Martin G. Pomper, Johns Hopkins Medical Institutions, 1550 Orleans Street, 492 CRB II, Baltimore, MD 21231. Phone: 410-955-2789; Fax: 443-817-0990; E-mail: mpomper@jhmi.edu.

doi:10.1158/1078-0432.CCR-07-1517

compound *N*-[*N*-[(*S*)-1,3-dicarboxypropyl]carbamoyl]-*S*-[^{11}C]methyl-L-cysteine ([^{11}C]DCMC) to one containing fluorine-18, *N*-[*N*-[(*S*)-1,3-dicarboxypropyl]carbamoyl]-4-[^{18}F]fluorobenzyl-L-cysteine ([^{18}F]DCFBC). Herein, we describe the synthesis, *in vivo* behavior, and human dosimetry estimates for [^{18}F]DCFBC.

Materials and Methods

N^{α}-Fmoc-*S*-*tert*-butyl-L-cysteine (**1**) was purchased from AnaSpec, Inc. All other reagents and solvents were purchased from either Sigma-Aldrich or Fisher Scientific. ^{1}H nuclear magnetic resonance (NMR) spectra were obtained on a Varian Mercury 400 MHz spectrometer. Optical rotation was measured on a Jasco P-1010 polarimeter. Mass spectrometry was done on a JOEL JMS-AX505HA mass spectrometer in the Mass Spectrometry Facility at the University of Notre Dame. Melting points were measured using a Mel-Temp apparatus and are uncorrected. High-performance liquid chromatography (HPLC) purification of (*S*)-2-[3-[(*R*)-1-carboxy-2-mercaptoethyl]ureido]-pentanedioic acid (**6**) and *N*-[*N*-[(*S*)-1,3-dicarboxypropyl]carbamoyl]-4-fluorobenzyl-L-cysteine (DCFBC) were done on a Waters 625 LC system with a Waters 490E Multiwavelength UV/Vis detector, both controlled by Millennium v2.10 software. Reverse-phase radio-HPLC analysis of 4-[^{18}F]fluorobenzyl-bromide (4-[^{18}F]FBB) was done using a Waters 610 HPLC pump, a Waters 441 fixed wavelength (254) UV detector, a Bioscan Flow-Count PIN diode radioactivity detector, a 3.9 × 150 mm 5 μm Nova Pak C-18 column, and a mobile phase of 40:60 (v/v) acetonitrile/0.1 mol/L aqueous ammonium formate. Chromatograms were analyzed using a Varian Galaxie Chromatography Data System version 1.8.501.1. Reverse-phase radio-HPLC semipreparative purification of [^{18}F]DCFBC was done using a Waters 510 pump, Waters 490E variable wavelength UV/Vis detector at 220 nm, a Bioscan Flow-Count PMT radioactivity detector, a 10 mm × 250 mm 10 μ Alltech Econosil C-18 column, and WinFlow (LabLogic) chromatography software. [^{18}F]KF was produced by 18 MeV proton bombardment of a high-pressure [^{18}O]H_2O target using a General Electric PETtrace biomedical cyclotron. Radioactivity was measured in Capintec 15R and CRC-12 dose calibrators. The specific radioactivity was calculated as the radioactivity eluting at the retention time of [^{18}F]DCFBC during the semipreparative HPLC purification divided by the mass corresponding to the area under the curve of the UV absorption.

Chemistry

N^{α}-*Fmoc*-S-tert-*butyl*-L-*cysteine*-4-*methoxybenzyl ester* (*2*). To a solution of 4.0 g (10 mmol) of N^{α}-Fmoc-*S*-*tert*-butyl-L-cysteine (**1**) dissolved in 80 mL of dry *N*, *N*-dimethylformamide (DMF) was added 6.5 g (20 mmol) of cesium carbonate and 2.4 g (15.3 mmol) of 4-methoxybenzyl chloride. The suspension was stirred at room temperature under nitrogen for 4 h. The suspension was filtered through a medium frit Büchner funnel and the solid was washed with CH_2Cl_2. The DMF and CH_2Cl_2 washes were combined and poured into 200 mL of ethyl acetate and extracted with 150 mL of water. The organic layer was washed twice with 150 mL of water, collected, dried over anhydrous magnesium sulfate, filtered, and concentrated on the rotary evaporator to give a colorless oil that solidified overnight. The solid was then recrystalized from 7:3 (v/v) hexane/ethyl acetate to give 3.4 g (65.5% yield) of a white solid (mp, 117-119°C). The filtrate was concentrated, dissolved in 2 mL of CH_2Cl_2, loaded onto a silica gel column, and eluted with 8:2 hexane/ethyl acetate to give an additional 0.7 g (13%) of product. TLC: silica gel on aluminum backing, 7:3 hexane/ethyl acetate, R_f = 0.66. ^{1}H NMR ($CDCl_3$) δ 7.77 (d, 2H, *J* = 6 Hz), 7.60 (d, 2H, *J* = 6 Hz), 7.40 (t, 2H, *J* = 7.5 Hz), 7.31 (m, 4H), 6.87 (d, 2H, *J* = 6.75 Hz), 5.64 (d, 1H, *J* = 7.5 Hz), 5.14 (d, 2H, *J* = 3 Hz), 4.68 (m, 1H), 4.37 (m, 2H), 4.22 (t, 1H, *J* = 7.5 Hz), 3.8 (s, 3H), 3.01 (d, 2H, *J* = 5 Hz), 1.28 (s, 9H). $[\alpha]^{24}_D$ (c 0.106, DMF) = -11.5; FAB+ *m/z* 520.2135 [MH$^+$].

S-tert-*butyl*-L-*cysteine*-4-*methoxybenzyl ester* (*3*). Thirty milliliters of a 20% solution of piperidine in DMF were added to 2.6 g (5 mmol) of N^{α}-Fmoc-*S*-*tert*-butyl-L-cysteine-4-methoxybenzyl ester (**2**) in a flame-dried round-bottomed flask. The reaction was stirred at room temperature for 10 to 15 min and poured into a separatory funnel containing 100 mL of CH_2Cl_2. This was extracted thrice with 50 mL of water followed by 100 mL of saturated NaCl. The organic layer was collected, dried over $MgSO_4$, filtered, and concentrated to a sticky white solid. The crude material was purified by flash column chromatography using silica gel and 1:1 hexane/ethyl acetate to give 1.26 g (85%) of a light yellow oil. TLC: 1:1 hexane/ethyl acetate, R_f = 0.38. ^{1}H NMR ($CDCl_3$) δ 7.25 (d, 2H, *J* = 7 Hz), 6.84 (d, 2H, *J* = 7 Hz), 5.10 (d, 2H, *J* = 3 Hz), 3.75 (s, 3H), 3.62 (dd, 1H, *J* = 3, 5 Hz), 2.88 (dd, 1H, *J* = 3.5, 9.7 Hz), 2.72 (dd, 1H, *J* = 5.5, 9.7 Hz), 1.72 (broad s, 2H), 1.26 (s, 9H). $[\alpha]^{24}_D$ (c 0.0318, DMF) = +3.4.

***Bis*-4-*methoxybenzylglutamate hydrochloride* (*4*).** Bis-4-methoxybenzylglutamate hydrochloride was prepared by the method of Maclaren (12) as a white solid (mp, 120-121°C; Lit., 114-115°C; ref. 12). ^{1}H NMR ($CDCl_3$) δ 7.23 (d, 2H, *J* = 6.4 Hz), 7.18 (d, 2H, *J* = 6.4 Hz), 6.81 (d, 2H, *J* = 2.8 Hz), 6.78 (d, 2H, *J* = 2.8 Hz), 5.06 (m, 2H), 4.93 (s, 2H), 4.29 (t, 1H, *J* = 5.2 Hz), 3.75 (s, 3H), 3.72 (s, 3H), 2.65 (m, 1H), 2.54 (m, 1H), 2.37 (m, 2H). $[\alpha]^{25}_D$ (c 0.195, DMF) = +3.1, Lit. (12) $[\alpha]^{20}_D$ (c 2, DMF) = +5.3.

***2*-{*3*-[*2*-Tert-*butylsulfanyl*-*1*-(*4*-*methoxy*-*benzyloxycarbonyl*)-*ethyl*]-*ureido*}-*pentanedioic acid bis*-(*4*-*methoxybenzyl*) *ester* (*5*).** A dry 250 mL round-bottomed flask was charged with 3.28 g (7.76 mmol) of bis-4-methoxybenzylglutamate hydrochloride (**4**) and dissolved in 45 mL of dry CH_2Cl_2 followed by cooling to -77°C under a nitrogen atmosphere. A solution of 0.77 g of triphosgene (2.59 mmol) dissolved in 8 mL of dry CH_2Cl_2 was added. A solution consisting of 2.3 mL of triethylamine (16.5 mmol) in 8 mL of dry CH_2Cl_2 was carefully added and the reaction was allowed to stir at -77°C for 1.5 h before warming to room temperature over 15 min. To this was added a solution containing 2.1 g (7.05 mmol) *S*-*tert*-butyl-L-cysteine-4-methoxybenzyl ester (**3**) dissolved in 13 mL of dry CH_2Cl_2. The mixture was stirred overnight at room temperature followed by extraction with CH_2Cl_2, two washes with water, and a wash with brine. The organic layer was collected, dried over Na_2SO_4, filtered, and concentrated to a thick oil. The crude material was purified on a silica gel column using 10:1 chloroform/ethyl acetate to give 3.75 g of a thick oil (75% yield from **4**). TLC: silica gel on aluminum backing, 10:1 chloroform/ethyl acetate, R_f = 0.49. ^{1}H NMR ($CDCl_3$) δ 7.28 to 7.22 (m, 6H), 6.88 to 6.84 (m, 6H), 5.9 to 5.6 (broad S, 2H), 5.08 (d, 4H, *J* = 3Hz), 5.0 (s, 2H), 4.76 (t, 1H, *J* = 4.5), 4.52 (dd, 1H, *J* = 4.5, 6Hz), 3.79 (s, 9H), 2.95 (t, 2H, *J* = 4.5), 2.38 (m, 2H), 2.15 (m, 1H), 1.95 (m, 1H), 1.23 (s, 9H). $[\alpha]^{25}_D$ (c 0.081, DMF) = -1.14.

***(S)*-*2*-[*3*-[(*R*)-*1*-*carboxy*-*2*-*mercaptoethyl*]*ureido*]-*pentanedioic acid* (*6*).** A 0°C solution containing 15 mL of trifluoroacetic acid (TFA) and 0.3 mL of anisole was added to a round-bottom flask containing 0.815 g (1.16 mmol) of **5**, and the mixture was stirred until **5** dissolved. To this solution was added 0.453 g (1.42 mmol) of mercuric acetate. The mixture was stirred at 0°C for 20 min followed by concentration at room temperature under reduced pressure. The mercury adduct was precipitated by the addition of ethyl ether, filtered, and then dried under reduced pressure to give 0.69 g of a fine white solid. This was used without further purification. The mercury adduct (0.69 g) was dissolved in 25 mL of DMF and H_2S was bubbled into this solution for 5 h. The resulting black slurry was filtered through filter agent (Celatom FW-14) and the filter agent was washed with methanol and water. Following concentration under reduced pressure, the product was then dissolved in methanol and filtered over glass paper, the filtrate was concentrated, and the process was repeated using water. The filtrate was then purified by reverse-phase HPLC (C-18 Econosil 10 × 250 mm preparative column; 95:5:0.1 H_2O/CH_3CN/TFA) to give 0.274 g (80%) of a light yellow–colored hygroscopic solid. ^{1}H NMR (CD_3OD) δ 4.53 (t, *J* = 5 Hz, 1H), 4.31 (dd, *J* = 5, 10 Hz, 1H), 2.93 (d, *J* = 4 Hz, 2H), 2.42 (m, 2H), 2.15 (m, 1H), 1.90 (m, 1H). Lit. ^{1}H NMR

(CD_3OD) δ 4.45 (t, J = 4.5 Hz, 1H), 4.21 (dd, J = 5, 8.5 Hz, 1H), 2.82 (d, J = 4.5 Hz, 2H), 2.31 (m, 2H), 2.05 (m, 1H), 1.80 (m, 1H); $[\alpha]_D^{24}$ +13.3 (c 0.0247, MeOH), Lit. (13) $[\alpha]_D^{20}$ +14.2 (c 0.12, MeOH); FAB+ m/z 295.0606 [MH^+].

***N*-[*N*-[(*S*)-1,3-dicarboxypropyl]carbamoyl]-4-fluorobenzyl-L-cysteine.** (*S*)-2-[3-[(*R*)-1-Carboxy-(4-fluorobenzylsulfanyl)ethyl]ureido] pentanedioic acid (**6**; 1.8 mg, 0.0061 mmol) and 4-fluorobenzyliodide (1.4 mg, 0.0061 mmol) were stirred in ammonia-saturated methanol (0.3 mL) at 60°C for 10 min and then acidified with TFA. Purification by reverse-phase HPLC (C-18 Econosil 10 × 250 mm preparative column; 32:68:0.1 CH_3CN/H_2O/TFA) gave pure product. ^1H NMR (CD_3OD) δ 7.35 (dd, 2H), 7.01 (dd, 2H), 4.49 (m, 1H), 4.32 (m, 1H), 3.78 (s, 2H), 2.84 (m, 2H), 2.42 (m, 2H), 2.15 (m, 1H), 1.92 (m, 1H). FAB m/z 401.0845 [M+H].

Radiochemistry

***N*-[*N*-[(*S*)-1,3-dicarboxypropyl]carbamoyl]-4-[^{18}F]fluorobenzyl-L-cysteine.** Typically, starting with 12.95 GBq (350 mCi) of [^{18}F]KF, a solution containing 91% 4-[^{18}F]FBB (14) was produced in 45 min [total reactivity, 3.4 GBq (93 mCi)] and placed in a 10 mL screw-cap borosilicate glass vial. To this solution (1.5 mL), still containing the brominating agent triphenylphosphine dibromide in methylene chloride/ether, was added two 4 mL volumes of diethyl ether to precipitate the triphenylphosphine dibromide. After standing for 1 min, the liquid phase was carefully transferred via a plastic pipette to a 16 × 150 mm borosilicate glass vial to which 800 μL methanol had been added previously. The liquid was concentrated under a stream of nitrogen at room temperature to ~200 μL. This solution was then added to a 4 mL borosilicate screw-cap glass vial containing an aqueous solution of (*S*)-2-[3-[(*R*)-1-carboxy-2-mercaptoethyl]ureido]-pentanedioic acid (**6**; 2-4 mg/40 μL). To this was added 200 μL of methanol previously saturated with ammonia gas. The vial was sealed and heated at 65°C for 10 min and then cooled for 2 min. To the reaction was added 600 μL water, 80 μL of TFA (a 5 μL sample was spotted on pH paper to confirm acidity), and 600 μL of HPLC mobile phase. The resulting product was then purified by reverse-phase semipreparative radio-HPLC using a mobile phase consisting of 35:65:0.1% acetonitrile/water/TFA and a flow rate of 4 mL/min, yielding 490 MBq (13.2 mCi) of [^{18}F]DCFBC eluting at 7 min. The product was concentrated under vacuum to dryness, reconstituted in 1 mL of PBS (pH 7.4), and filtered through a 0.22 μm syringe filter into an evacuated sterile vial.

In vitro *inhibition assay*. Taking advantage of the *N*-acetylaspartylglutamate (NAAG) peptidase activity of PSMA, the relative affinity of DCFBC for PSMA was determined using a previously published NAAG peptidase assay (15). Briefly, NAAG peptidase activity was determined using membranes of CHO cells stably transfected with NAAG peptidase (also known as PSMA), 4 μmol/L NAAG as a substrate, and a trace amount of [^{3}H]NAAG. Inhibitors at concentrations of 0.1, 1, 10, and 100 nmol/L were tested. Product was separated using ion exchange chromatography (AG-50W-X8 analytic-grade cation exchange resin). The amount of [^{3}H]glutamate as a product of NAAG hydrolysis was determined by scintillation spectrophotometry.

Cell lines and mouse models

PC-3 PIP ($PSMA^+$) and PC-3 FLU ($PSMA^-$) cell lines were obtained from Dr. Warren Heston (Cleveland Clinic, Cleveland, OH) and maintained as previously described (16). All cells were grown to 80% to 90% confluency before trypsinization and formulation in HBSS (Sigma-Aldrich) for implantation into mice.

All animal studies were carried out in full compliance with institutional guidelines related to the conduct of animal experiments. Male severe combined immunodeficient mice (Charles River Laboratories) were implanted s.c. with 1×10^6 to 5×10^6 cells forward of each shoulder. PC-3 PIP cells were implanted behind the left shoulder and PC-3 FLU cells were implanted behind the right shoulder. Mice were imaged or used in biodistribution assays when the tumor xenografts reached 3 to 5 mm in diameter.

Rodent biodistribution

The xenograft-bearing mice (17-20 g) were injected via the tail vein with 3.70 MBq (100 μCi, 286 pmol, 350 Ci/mmol) of [^{18}F]DCFBC in 200 μL of saline. Blood was collected immediately after sacrifice (cervical dislocation) by cardiac puncture and heart, lung, liver, stomach, pancreas, spleen, white fat, kidney, bone, muscle, small intestine, large intestine, urinary bladder, tumor xenografts, cerebral cortex, and cerebellum were harvested, weighed, and counted in an automated gamma counter (LKB Wallace 1282 Compugamma CS Universal Gamma Counter). Animals were sacrificed at 5, 15, 30, 60, and 120 min after injection (n = 4 per time point). Tissue radiopharmaceutical uptake values were calculated as percent injected dose per gram (% ID/g) compared with a 1:10 diluted standard dose. The urinary bladder was emptied and water washed and then dried before weighing and counting.

Small-animal PET

A severe combined immunodeficient mouse bearing s.c. PC-3 PIP and PC-3 FLU xenografts was anesthetized using 3% isoflurane in oxygen for induction and 1.5% isoflurane in oxygen at 0.8 L/min flow for maintenance and positioned prone on the gantry of a GE eXplore Vista small-animal PET scanner (GE Healthcare). The mouse was injected i.v. with 7.4 MBq (200 μCi, 572 pmol, 350 Ci/mmol) of [^{18}F]DCFBC followed by image acquisition using the following protocol: The images were acquired as a pseudodynamic scan (i.e., a sequence of successive whole-body images acquired in two bed positions for a total of 2 h). The dwell time at each position was 5 min such that a given bed position (or mouse organ) was revisited every 10 min. An energy window of 250 to 700 keV was used. Images were reconstructed using the FORE/2D-OSEM method (2 iterations, 16 subsets) and included corrections for radioactive decay, scanner dead time, and scattered radiation.

Human dosimetry estimates

Dosimetry values were calculated using mouse biodistribution data. The mouse activity values in %ID/g were converted to human %ID/organ by setting the ratio of organ %ID/g to whole-body %ID/g in the mouse equal to that in humans and then solving for human %ID/organ; the adult male organ masses listed in the software code OLINDA were used (17). Cumulative activity per injected activity for each organ was obtained by numerically integrating over the existing time points and then fitting a monoexponential curve to the last three time points to extrapolate effective clearance rate beyond the last measured time point. The sum of the numerical (measured data) and the analytic integrals gave the total cumulated activity. This was divided by the amount of activity administered to give cumulated activity per unit activity. The resulting residence times in MBq-h/MBq were entered into OLINDA to calculate absorbed and effective doses. DCFBC is a small molecule whose concentration in blood is not readily related to that in marrow. The red marrow was not directly sampled. The absorbed dose to red marrow is therefore the cross-fire dose from all activity containing sources in the body; this includes activity in the trabecular bone, which was directly measured, and blood (assigned to rest of body term). Values for residence times in the lower large intestine, small intestine, stomach, upper large intestine, and urinary bladder all reflect the contents as well as the tissue of the indicated organs.

Results

Chemistry and PSMA inhibition. Figure 1 depicts the synthesis of DCFBC and [^{18}F]DCFBC. The synthesis of **6** is a modification of the route previously described by Kozikowski et al. (13) where the benzyl protecting groups are now replaced by the acid labile *p*-methoxybenzyl groups. In particular, the carboxyl group of commercial N^{α}-Fmoc-*S*-*tert*-butyl-L-

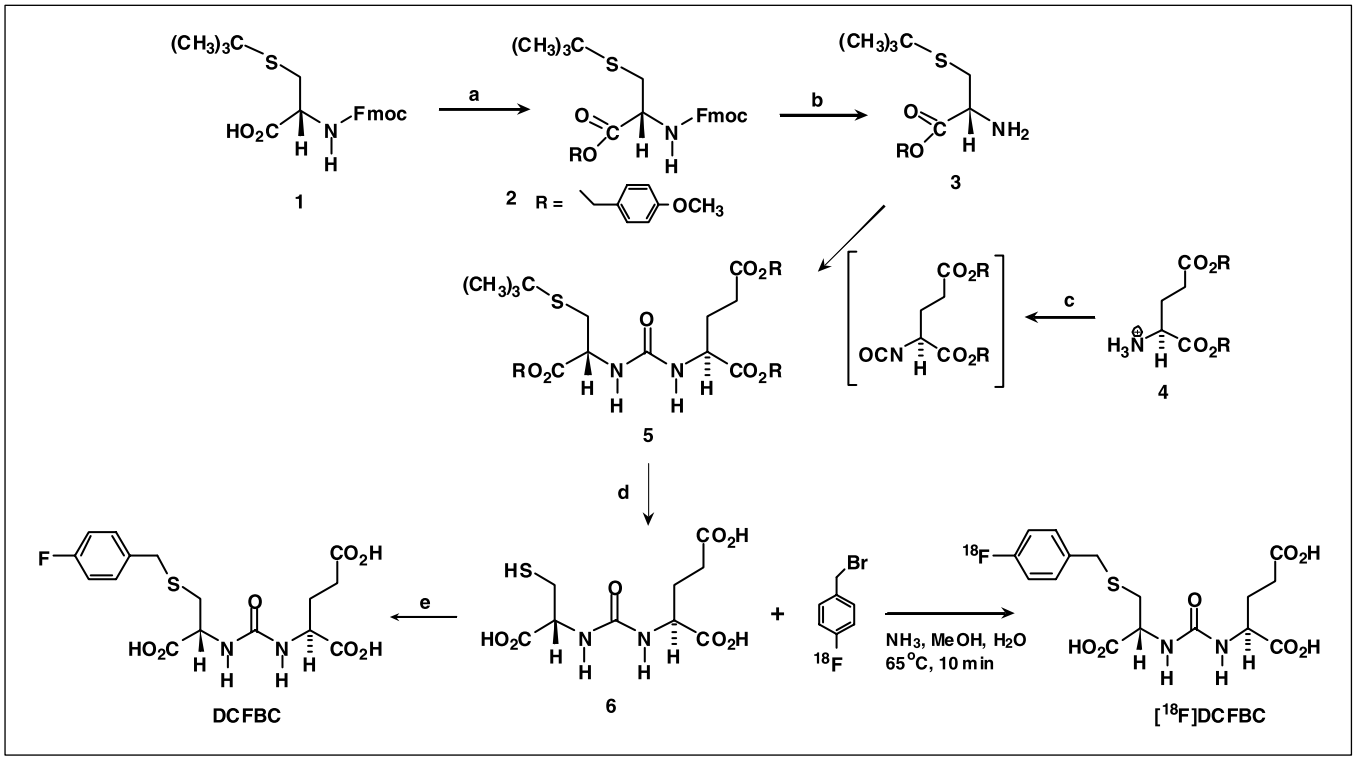

Fig. 1. a, 4-methoxybenzyl chloride, Cs_2CO_3, DMF. b, 20% piperidine, DMF. c, triphosgene, triethylamine followed by **3**. d, **1**, TFA, anisole, $Hg(OAc)_2$; **2**, H_2S. e, ammonia-saturated methanol, 4-fluorobenzyl iodide.

cysteine (**1**) is protected as a *p*-methoxybenzyl ester to give **2**. The Fmoc group is removed, giving amine **3**, which is then reacted with the isocyanate formed from bis-4-methyoxybenzyl glutamate hydrochloride **4** (12) to give urea **5**. Cleavage of all remaining protecting groups gives precursor **6**.

The fluorine-18–labeled prosthetic group 4-[^{18}F]FBB was prepared by the method of Ravert et al. (14) and reacted with **6** in ammonium-saturated methanol at 60°C for 10 min followed by acidification and purification by reverse-phase radio-HPLC. The average uncorrected yield of [^{18}F]DCFBC from [^{18}F]FBB was 16 ± 6% (n = 8). In a typical experiment, the non–decay-corrected yield of the total synthesis from [^{18}F]KF was 3.5% in 123 min (decay-corrected yield was 7.6%). The specific radioactivities ranged from 13 to 133 GBq/μmol (350-3,600 Ci/mmol) with an average of 52 GBq/μmol (1,492 Ci/mmol; n = 6). The range of specific radioactivities,

Table 1. Tissue distribution of [^{18}F]DCFBC

Tissue	%ID/g ± SD (n = 4)				
	5 min	15 min	30 min	60 min	120 min*
Blood	11.3 ± 6.7	4.1 ± 2.5	2.3 ± 1.3	1.8 ± 1.4	0.4 ± 0.2
Heart	4.4 ± 0.9	2.0 ± 0.6	1.2 ± 0.2	0.8 ± 0.3	0.3 ± 0.2
Lung	7.0 ± 0.5	3.2 ± 0.9	1.8 ± 0.3	1.1 ± 0.4	0.4 ± 0.1
Liver	6.0 ± 1.2	4.1 ± 1.4	4.2 ± 0.5	5.1 ± 0.8	2.1 ± 1.4
Stomach	2.9 ± 0.3	1.4 ± 0.3	0.8 ± 0.1	0.5 ± 0.2	1.1 ± 1.9
Spleen	8.8 ± 1.3	4.3 ± 1.4	1.9 ± 0.9	1.6 ± 0.9	0.4 ± 0.2
Fat	1.8 ± 0.4	1.6 ± 1.0	0.7 ± 0.5	1.0 ± 0.7	0.3 ± 0.1
Kidney	63.4 ± 8.2	63 ± 20	51.3 ± 7.5	41.6 ± 7.2	13 ± 10
Bone	2.9 ± 0.4	1.6 ± 0.3	1.7 ± 0.1	1.7 ± 0.8	2.5 ± 3.6
Muscle	2.2 ± 1.0	1.0 ± 0.4	0.5 ± 0.1	0.6 ± 0.5	0.2 ± 0.4
Small intestine	4.3 ± 0.4	2.3 ± 1.3	1.2 ± 0.2	0.7 ± 0.2	0.2 ± 0.1
Large intestine	2.8 ± 0.4	1.5 ± 0.7	0.8 ± 0.1	0.6 ± 0.2	0.3 ± 0.1
Bladder (empty)	55 ± 30	16 ± 15	15 ± 15	14.5 ± 7.3	2.6 ± 1.0
PC-3 FLU tumor	3.5 ± 0.5	1.7 ± 0.4	1.0 ± 0.1	0.8 ± 0.2	0.2 ± 0.0
PC-3 PIP tumor	8.2 ± 0.8	6.0 ± 2.6	6.2 ± 1.0	8.2 ± 2.5	4.7 ± 0.9

*n = 3.

Table 2. PC-3 PIP tumor to tissue ratios

Tissue	5 min	15 min	30 min	60 min	120 min*
Blood	0.7	1.5	2.7	4.5	13
Heart	1.9	3.0	5.0	10	17
Lung	1.2	1.9	3.5	7.4	30
Liver	1.4	1.5	1.5	1.6	2.2
Stomach	2.8	4.5	7.6	18	4.3
Spleen	0.9	1.4	3.2	5.2	11
Fat	4.7	3.9	9.2	7.8	18
Kidney	0.1	0.1	0.1	0.2	0.4
Bone	2.8	3.8	3.6	4.7	1.9
Muscle	3.7	6.0	14	14	20
Small intestine	1.9	2.6	5.1	12	31
Large intestine	2.9	4.1	7.9	14	17
Bladder (empty)	0.15	0.4	0.4	0.6	1.8
FLU tumor	2.4	3.5	6.4	11	27

*n = 3.

although wide, represents data from all syntheses done, including the first. However, even with this unoptimized manual technique, we have been able to achieve specific radioactivities that should be sufficient for human studies.

A NAAG peptidase inhibition assay (15) was undertaken to determine the IC_{50} value for DCFBC and thus its inhibitory capacity for PSMA. The concentration of DCFBC was varied from 1 to 100 nmol/L against a fixed amount of NAAG (4 μmol/L) and a trace amount of [^{3}H]NAAG. The NAAG peptidase (PSMA) was prepared from lysed PSMA-transfected CHO cells. The percent enzymatic cleavage product, [^{3}H]glutamate, was measured by scintillation counting and plotted against the logarithmic concentration of DCFBC. Linear regression of the resulting data was solved for 50% [^{3}H]glutamate (50% inhibition) and resulted in an IC_{50} value of 13.9 nmol/L for DCFBC. That result is in keeping with other compounds of this class (7, 8, 13).

Rodent biodistribution and PET imaging. Table 1 outlines the *ex vivo* rodent tissue distribution results. The blood, kidney, urinary bladder, spleen, and PSMA$^+$ PC-3 PIP tumor display high uptake at the initial 5-min postinjection time point. By 60 min after injection, the kidneys and urinary bladder display the highest uptake, while the uptake in PSMA$^+$ PC-3 PIP tumor achieves its highest absolute value. The values noted in the kidney are partially due to specific binding (18, 19) but are likely dominated by renal clearance because washout was much faster from kidney than PC-3 PIP tumor. Urinary bladder uptake represents excretion at all time points (i.e., there was no specific binding to bladder wall), whereas tumor uptake shows a high degree of specificity represented by the PIP to FLU uptake ratio of 10:1 at 60 min and rising to 20:1 at 120 min (Table 2). Tumor to other organ ratios also increase with time.

Figure 2 shows the PET scans at specific time intervals. Specific uptake in PSMA$^+$ PIP tumor is clearly seen as early as the 20- to 30-min image. Clearance from nontarget tissues is evident at later time points. By 2 h, radioactivity in the kidney is confined to cortex. The renal activity steadily decreased throughout the time course investigated and did so more rapidly than in other tissues, including the PIP tumors (Fig. 3). Although the blood curve seems to decrease from 30 to 60 min, those from liver and tumor seem to rise. That is an unexpected and likely artifactual result due to the large SE in determining the %ID/g in those tissues. Little nonspecific tissue radioactivity uptake is evident. Renal excretion dominates with this hydrophilic compound.

Human dosimetry estimates. Table 3 indicates human dosimetry estimates for [^{18}F]DCFBC. Tables 3 and 4 list the absorbed doses and residence times, respectively, estimated from the mouse biodistribution data. The highest absorbed dose was to the kidneys [0.05 mGy/MBq (0.2 rad/mCi)].

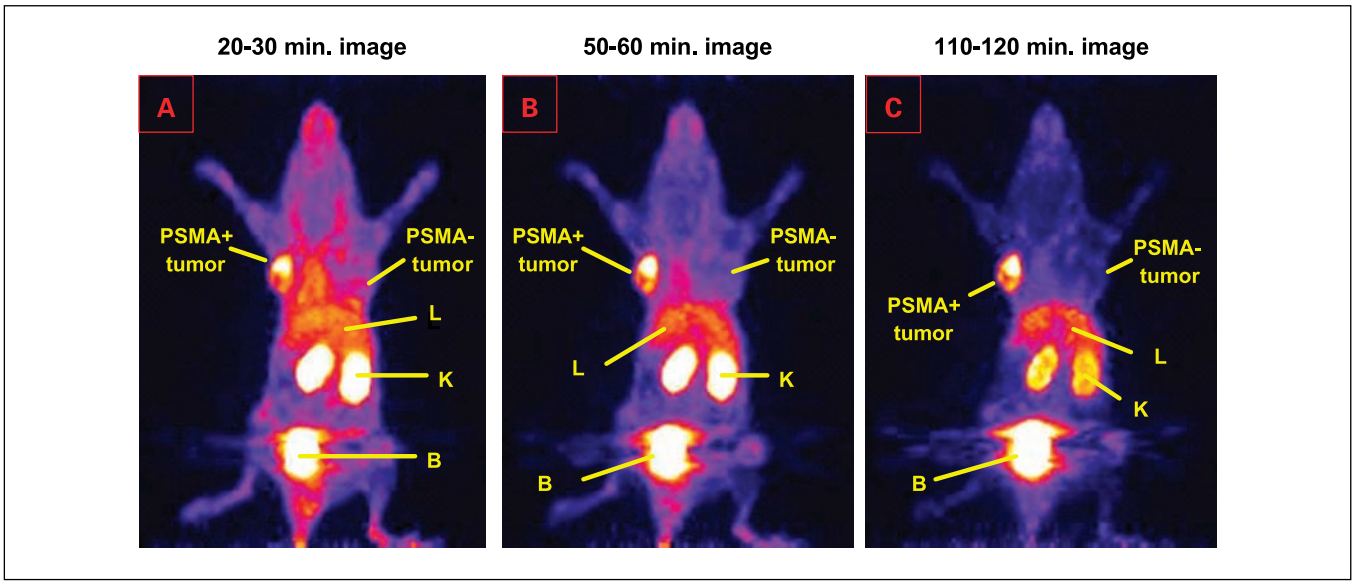

Fig. 2. GE eXplore Vista dynamic PET images. Animals were injected with 7.4 MBq (200 μCi, 572 pmol, 350 Ci/mmol) of [^{18}F]DCFBC before imaging. Summation images from the indicated time frames are shown. The PSMA$^+$ PC-3 PIP tumor is under the left shoulder, whereas the PSMA$^-$ PC-3 tumor is under the right shoulder. Note accumulation of [^{18}F]DCFBC only within the target-containing tumor. Radioactivity intensifies within the tumor and begins to wash out of the kidneys on the time scale shown.

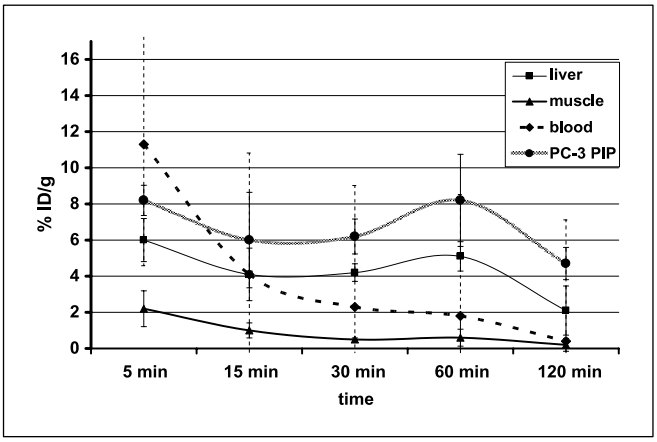

Fig. 3. Time-activity curves of [^{18}F]DCFBC biodistribution in selected tissues (*ex vivo* analysis). Animals were injected with 3.70 MBq (100 μCi, 286 pmol, 350 Ci/mmol) of [^{18}F]DCFBC before sacrifice and harvest of the indicated tissues. There is a peak of radioactivity within tumor and muscle at 60 min after injection before washout (n = 3).

Excluding the kidneys, mean absorbed doses ranged from 0.009 (liver) to 0.0005 (brain) mGy/MBq (0.035-0.002 rad/mCi). The effective dose equivalent and effective doses were 0.005 and 0.003 mSv/MBq, respectively.

Discussion

Prostate cancer is the most common solid tumor in men (20). Testing for PSA in serum can suggest the presence or recurrence of tumor but provides no spatial information, which dictates therapy. Although it is true that nomograms, composed of clinical variables such as PSA level and velocity, have proved useful in predicting local extension, they do less well in predicting lymph node involvement (21). In fact, lymph node involvement is often underestimated in prostate cancer and detection of such involvement, or involvement of other metastatic sites, could obviate unnecessary surgery (21, 22). One study found that 4.5% of patients who underwent abdominoperineal resection for colorectal cancer had perirectal lymph nodes that contained prostate cancer (23). In brief, to predict outcome, provide image-guided therapy, and facilitate therapeutic monitoring, an imaging agent capable of detecting prostate cancer with high specificity and sensitivity is needed. As discussed in Introduction, certain mechanism-based agents are under investigation, including a magnetic resonance imaging–based agent that has tremendous promise in detecting nodal disease (24). However, only ProstaScint has gained Food and Drug Administration approval. ProstaScint has not been as widely implemented as hoped primarily due to suboptimal pharmacokinetics. High-resolution single-photon emission computed tomography devices coupled with fused imaging have improved the detection of metastatic deposits with ProstaScint; however, accuracy remains at 83%, leaving room for improvement (21). Furthermore, results obtained with ProstaScint have been controversial, with some reports claiming no advantage in using the scan in patients who are postprostatectomy with rising PSA (25).

Like ProstaScint, [^{18}F]DCFBC binds to PSMA, the most well-established and highly restricted prostate cancer–related membrane antigen (26). PSMA is up-regulated in prostate cancer, particularly in advanced, hormone-independent, and metastatic disease (27, 28). It is also expressed in the neovasculature of nearly all solid tumors (10, 11). Because it is an integral membrane protein with an enzymatic active site in an extracellular domain, it provides an ideal target for imaging and therapy. Adding further to the attractiveness of PSMA as an imaging target is its limited pattern of expression, primarily within prostate, small bowel, proximal renal tubule, and brain (19). PSMA is an active target for the development of imaging agents for prostate cancer, and therapeutic agents for psychiatric disease, with several reviews having recently appeared (29–32). There is an emerging literature on the development of inhibitors for PSMA, which is expected to increase with the recent availability of a high-resolution crystal structure of the enzyme (13, 33–35). We and others have synthesized radiopharmaceuticals and optical agents for PSMA detection (7–9, 36, 37), with [^{18}F]DCFBC representing the first agent designed specifically for clinical PET imaging of prostate cancer.

[^{18}F]DCFBC localized selectively to the PSMA$^+$ prostate tumor, PC-3 PIP (Fig. 2; Tables 1 and 2), achieving a target/background (muscle) ratio of 20:1 at 120 min after injection. The time-activity curves indicate that [^{18}F]DCFBC has achieved equilibrium by 120 min and has begun to decrease in concentration at the target site. Washout from target was slower than from nontarget sites. Notably, the criteria for ProstaScint to progress to the clinic required a 3:1 tumor/muscle ratio in s.c. LNCaP tumors, and a similar uptake ratio shown in the clinic provided a positive predictive value for the presence of prostate cancer at >90% (38). [^{18}F]DCFBC did not show significant defluorination, as evidenced by the low levels of bone uptake. That is particularly important because of the propensity prostate cancer has for metastasizing to bone. The 1-h PIP/bone value was 4.7, suggesting that metastatic lesions, which are known to express PSMA, will be clearly delineated (11, 39).

As seen for our initial PET radioligand, [^{11}C]DCMC (7), there is significant uptake within kidney that is due, at least in part, to specific binding to proximal renal tubules. We have shown this

Table 3. Radiation absorbed doses

	Total absorbed doses (mGy/MBq)
Brain	4.97E-04
Lower large intestinal wall	1.01E-03
Small intestine	1.45E-03
Stomach wall	1.57E-03
Upper large intestinal wall	1.53E-03
Heart wall	2.25E-03
Kidneys	4.87E-02
Liver	9.34E-03
Lungs	2.58E-03
Muscle	1.37E-03
Pancreas	3.03E-03
Red marrow	3.12E-03
Spleen	4.25E-03
Urinary bladder wall	8.99E-04
Total body	1.79E-03

NOTE: Estimate reflects dose contribution from other organs. Absorbed dose values in mGy/MBq per organ expected in average human.

Table 4. Radiation residence times

Brain	8.76E-04
Lower large intestine	1.01E-03
Small intestine	4.00E-03
Stomach	6.20E-04
Upper large intestine	1.01E-03
Heart wall	1.94E-03
Kidneys	7.85E-02
Liver	6.78E-02
Lungs	9.39E-03
Muscle	8.41E-02
Pancreas	3.66E-04
Trabecular bone	5.24E-02
Spleen	2.19E-03
Urinary bladder contents	3.98E-03
Remainder	7.37E-02

NOTE: The residence times obtained for each organ in an average human reported in MBq-h/MBq.

with other agents that we have developed for single-photon emission computed tomography imaging of PSMA (data not shown). Because of the presumed high renal exposure, we undertook dosimetry studies that indicate an exposure of 0.0487 mGy/MBq, which is within accepted levels (Table 3). The estimated absorbed doses resulting from expected administration of 185 to 370 MBq (5-10 mCi) of [^{18}F]DCFBC are acceptable for nuclear medicine diagnostic procedures (Table 3). Vallabhajosula et al. (40) have reported on the dosimetry of the anti-PSMA antibody, J591, labeled with indium-111. Using imaging and serial blood data obtained from a phase I study, they found that liver received the greatest absorbed dose at 1.1 mGy/MBq and the kidneys received the third greatest absorbed dose at 0.7 mGy/MBq. The absorbed doses for [^{18}F]DCFBC are 1 to 2 orders of magnitude below the values reported for [^{111}In]J591.

In summary, we have synthesized the first clinically practical PET imaging agent for PSMA. [^{18}F]DCFBC has a suitable physical half-life and appropriate pharmacokinetics and dosimetry and can be synthesized with relative ease in reasonable radiochemical yield and specific radioactivity. Together with the development of standard operating procedures for radiosynthesis according to good manufacturing practice, toxicity studies are under way toward clinical implementation.

Disclosure of Potential Conflicts of Interest

No potential conflicts of interest were disclosed.

References

1. Jemal A, Murray T, Samuels A, Ghafoor A, Ward E, Thun MJ. Cancer statistics, 2003. CA Cancer J Clin 2003;53:5–26.
2. Oehr P, Bouchelouche K. Imaging of prostate cancer. Curr Opin Oncol 2007;19:259–64.
3. de Jong IJ, Pruim J, Elsinga PH, Vaalburg W, Mensink HJ. ^{11}C-choline positron emission tomography for the evaluation after treatment of localized prostate cancer. Eur Urol 2003;44:32–8; discussion 8–9.
4. Price DT, Coleman RE, Liao RP, Robertson CN, Polascik TJ, DeGrado TR. Comparison of [^{18}F]fluorocholine and [^{18}F]fluorodeoxyglucose for positron emission tomography of androgen dependent and androgen independent prostate cancer. J Urol 2002;168:273–80.
5. Larson SM, Morris M, Gunther I, et al. Tumor localization of 16β-^{18}F-fluoro-5α-dihydrotestosterone versus ^{18}F-FDG in patients with progressive, metastatic prostate cancer. J Nucl Med 2004;45:366–73.
6. Nagda SN, Mohideen N, Lo SS, et al. Long-term follow-up of ^{111}In-capromab pendetide (ProstaScint) scan as pretreatment assessment in patients who undergo salvage radiotherapy for rising prostate-specific antigen after radical prostatectomy for prostate cancer. Int J Radiat Oncol Biol Phys 2007;67:834–40.
7. Pomper MG, Musachio JL, Zhang J, et al. ^{11}C-MCG: synthesis, uptake selectivity, and primate PET of a probe for glutamate carboxypeptidase II (NAALADase). Mol Imaging 2002;1:96–101.
8. Foss CA, Mease RC, Fan H, et al. Radiolabeled small molecule ligands for prostate-specific membrane antigen: *in vivo* imaging in experimental models of prostate cancer. Clin Cancer Res 2005;11:4022–8.
9. Dusich CA, Mease RC, Foss CA, Pomper MG. General approach for the preparation of fluorescent PSMA/GCPII inhibitors. In: 5th Annual Meeting of the Society for Molecular Imaging, 2006. Kona (HI); 2006.
10. Kinoshita Y, Kuratsukuri K, Landas S, et al. Expression of prostate-specific membrane antigen in normal and malignant human tissues. World J Surg 2006;30:628–36.
11. Milowsky MI, Nanus DM, Kostakoglu L, et al. Vascular targeted therapy with anti-prostate-specific membrane antigen monoclonal antibody J591 in advanced solid tumors. J Clin Oncol 2007;25:540–7.
12. Maclaren J. Some amino acid esters—an improved preparative method. Aust J Chem 1978;31:1865–8.
13. Kozikowski AP, Nan F, Conti P, et al. Design of remarkably simple, yet potent urea-based inhibitors of glutamate carboxypeptidase II (NAALADase). J Med Chem 2001;44:298–301.
14. Ravert HT, Madar I, Dannals RF. Radiosynthesis of 3-[^{18}F]fluoropropyl and 4-[^{18}F]fluorobenzyl triarylphosphonium ions. J Label Compd Radiopharm 2004;47:469–76.
15. Bzdega T, Turi T, Wroblewska B, et al. Molecular cloning of a peptidase against *N*-acetylaspartylglutamate from a rat hippocampal cDNA library. J Neurochem 1997;69:2270–7.
16. Chang SS, Reuter VE, Heston WD, Bander NH, Grauer LS, Gaudin PB. Five different anti-prostate-specific membrane antigen (PSMA) antibodies confirm PSMA expression in tumor-associated neovasculature. Cancer Res 1999;59:3192–8.
17. Stabin MG, Sparks AB, Crowe EB, Cremonesi M, Siegel JA. Olinda/Exm 1.0 and Radar. Eur J Nucl Med Mol Imaging 2004;31:S471.
18. Slusher BS, Tsai G, Yoo G, Coyle JT. Immunocytochemical localization of the N-acetyl-aspartyl-glutamate (NAAG) hydrolyzing enzyme N-acetylated α-linked acidic dipeptidase (NAALADase). J Comp Neurol 1992;315:217–29.
19. Silver DA, Pellicer I, Fair WR, Heston WD, Cordon-Cardo C. Prostate-specific membrane antigen expression in normal and malignant human tissues. Clin Cancer Res 1997;3:81–5.
20. Keane TE, Rosner IL, Wingo MS, McLeod DG. The emergence of radioimmunoscintigraphy for prostate cancer. Rev Urol 2006;8 Suppl 1:S20–8.
21. Manyak MJ, Javitt M, Kang PS, Kreuger WR, Storm ES. The evolution of imaging in advanced prostate cancer. Urol Clin North Am 2006;33:133–46, v.
22. Bader P, Burkhard FC, Markwalder R, Studer UE. Disease progression and survival of patients with positive lymph nodes after radical prostatectomy. Is there a chance of cure? J Urol 2003;169:849–54.
23. Murray SK, Breau RH, Guha AK, Gupta R. Spread of prostate carcinoma to the perirectal lymph node basin: analysis of 112 rectal resections over a 10-year span for primary rectal adenocarcinoma. Am J Surg Pathol 2004;28:1154–62.
24. Harisinghani MG, Barentsz J, Hahn PF, et al. Noninvasive detection of clinically occult lymph-node metastases in prostate cancer. N Engl J Med 2003;348:2491–9.
25. Nargund V, Al Hashmi D, Kumar P, et al. Imaging with radiolabelled monoclonal antibody (MUJ591) to prostate-specific membrane antigen in staging of clinically localized prostatic carcinoma: comparison with clinical, surgical and histological staging. BJU Int 2005;95:1232–6.
26. Bander NH. Technology insight: monoclonal antibody imaging of prostate cancer. Nat Clin Pract Urol 2006;3:216–25.
27. Schulke N, Varlamova OA, Donovan GP, et al. The homodimer of prostate-specific membrane antigen is a functional target for cancer therapy. Proc Natl Acad Sci U S A 2003;100:12590–5.
28. Huang X, Bennett M, Thorpe PE. Anti-tumor effects and lack of side effects in mice of an immunotoxin directed against human and mouse prostate-specific membrane antigen. Prostate 2004;61:1–11.
29. Zhou J, Neale JH, Pomper MG, Kozikowski AP. NAAG peptidase inhibitors and their potential for diagnosis and therapy. Nat Rev Drug Discov 2005;4:1015–26.
30. Baslow MH. NAAG peptidase as a therapeutic target: potential for regulating the link between glucose metabolism and cognition. Drug News Perspect 2006;19:145–50.
31. Thomas AG, Wozniak KM, Tsukamoto T, et al. Glutamate carboxypeptidase II (NAALADase) inhibition as a novel therapeutic strategy. Adv Exp Med Biol 2006;576:327–37; discussion 61–3.
32. Jackson PF, Slusher BS. Design of NAALADase inhibitors: a novel neuroprotective strategy. Curr Med Chem 2001;8:949–57.

33. Barinka C, Starkova J, Konvalinka J, Lubkowski J. A high-resolution structure of ligand-free human glutamate carboxypeptidase II. Acta Crystallograph Sect F Struct Biol Cryst Commun 2007;63:150–3.

34. Ding P, Helquist P, Miller MJ. Design, synthesis and pharmacological activity of novel enantiomerically pure phosphonic acid-based NAALADase inhibitors. Org Biomol Chem 2007;5:826–31.

35. Majer P, Jackson PF, Delahanty G, et al. Synthesis and biological evaluation of thiol-based inhibitors of glutamate carboxypeptidase II: discovery of an orally active GCP II inhibitor. J Med Chem 2003;46:1989–96.

36. Humblet V, Lapidus R, Williams LR, et al. High-affinity near-infrared fluorescent small-molecule contrast agents for *in vivo* imaging of prostate-specific membrane antigen. Mol Imaging 2005;4:448–62.

37. Humblet V, Misra P, Frangioni JV. An HPLC/mass spectrometry platform for the development of multimodality contrast agents and targeted therapeutics: prostate-specific membrane antigen small molecule derivatives. Contrast Media Mol Imaging 2006;1:196–211.

38. Tasch J, Gong M, Sadelain M, Heston WD. A unique folate hydrolase, prostate-specific membrane antigen (PSMA): a target for immunotherapy? Crit Rev Immunol 2001;21:249–61.

39. Barwe SP, Maul RS, Christiansen JJ, et al. Preferential association of prostate cancer cells expressing prostate specific membrane antigen to bone marrow matrix. Int J Oncol 2007;30:899–904.

40. Vallabhajosula S, Kuji I, Hamacher KA, et al. Pharmacokinetics and biodistribution of ^{111}In- and ^{177}Lu-labeled J591 antibody specific for prostate-specific membrane antigen: prediction of 90Y-J591 radiation dosimetry based on ^{111}In or ^{177}Lu? J Nucl Med 2005;46:634–41.